Northumbria Research Link

Designing graded fuel cell electrodes for proton exchange membrane (PEM) fuel cells with recurrent neural network (RNN) approaches

Hanhui Lei[a], Lei Xing[b]*, Hai Jiang[a], Yucheng Wang[a], Ben Bin Xu[a], Jin Xuan[b]*,

Terence Xiaoteng Liu[a]*

[a.] Faculty of Engineering and Environment, Northumbria University, Newcastle upon Tyne, NE1 8ST, United Kingdom

[b.] Department of Chemical and Process Engineering, University of Surrey, Guildford GU2 7XH, UK

To whom correspondence should be addressed:

Dr. Lei Xing l.xing@surrey.ac.uk

Prof. Jin Xuan j.xuan@surrey.ac.uk

Dr. Xiaoteng Liu: terence.liu@northumbria.ac.uk

Abstract: The graded distribution of Pt loading in the catalyst layer (CL) and the porosity of the gas diffusion layer (GDL) significantly affect the spatial distributions of electrochemical reaction and mass transport rates, thus influencing the cell performance and durability. A sophisticated physics-based model is established to study the influence of graded Pt loading and GDL porosity at the cathode, with their distribution function obeying the elliptic equation along the in-plane and through-plane directions, on the current density and its uniformity at a given cell voltage. To reduce the computational time and resources, an RNN algorithm-based data-driven surrogate model is developed to assist in the identification of the relationship between the design parameters and the objective functions. Latin hypercube sampling (LHS) method is implemented for sampling and then the initial data acquisition is conducted for training and testing the surrogate model. Results show that the machine learning (ML) algorithm could effectively assist the optimal design of the functionally graded electrode, and the surrogate model achieves > 97.9% prediction accuracy for current density and < 0.13 root mean square error (RMSE) for current homogeneity. Both the individual variation of Pt loading and GDL porosity and their interaction are respectively analysed. Results also indicate that the inhomogeneous Pt distribution improves the current density. On the contrary, GDL porosity has a greater impact on the cell performance since current density monotonically increases with the homogeneous GDL porosity. When both the inhomogeneous distributions of Pt loading and GDL porosity are simultaneously considered, the homogeneity of current density is improved. However, the improvement of the homogeneity of current density (increases by 54%) sacrifices the maximum current density (reduces by 22%).

1. Introduction

Hydrogen energy, as a kind of efficient and clean energy, can simultaneously alleviate the energy crisis and reduce environmental pollution and has become the focus of global renewable energy development [1, 2]. Hydrogen-powered polymer electrolyte membrane fuel cells (PEMFCs) with the advantages of high chemical to electrical energy conversion efficiency, low operating temperature, and near-zero pollution have been widely researched and developed to be the most suitable power source for electric vehicles (EV) [3], aviation [4], residential backup power [5], as well as energy storage applications up to grid-scale [6]. During PEMFCs operation, reactant gases flow along the channels within the bipolar plates, diffuse through the gas diffusion layer (GDL) and reach the active catalyst sites along with the catalyst layer (CL). From an energy engineering aspect, one of the main challenges of PEMFCs is the inhomogeneous power density distribution within the electrode because the molar concentrations of hydrogen and oxygen are generally higher at the gas inlets and channel-GDL interface and gradually decrease along the channels and through the porous electrode due to the consumption of the reactants, which leads to a low concentration of reactants near the gas outlet and membrane-CL interface and induces inhomogeneous mass transfer. In a traditional PEMFC, the catalysts are evenly spray-coated on the GDL or membrane to form a three-dimensional CL architecture. However, for PEMFCs operated at different loads, the required reaction activities and mass transport rates are different owing to the non-uniform distributions of reactants and products [7]. Considering the power per catalyst loading for each unit of the electrode, it is concluded that the catalysts near the gas outlet and away from the channel-GDL interface are not fully utilised, leading to a waste of precious metal nanoparticles, e.g., Pt/C. Thus, the design of inhomogeneous porous electrodes is a promising strategy to save the usage of precious metal catalysts and achieve a more uniform distribution of current density without sacrificing the performance of PEMFCs.

The sluggish reaction that occurs in PEMFCs is the oxygen reduction reaction (ORR) at the cathode side, which converts O_2 to two - O on the catalyst surface active sites. Commercially available active carbon supported Pt-group precious metals nanoparticles have been widely

3

used as the catalyst which enhances the reaction rate, but the cost is also dramatically increased [8, 9]. It is necessary to improve the utilisation and efficiency of Pt-based catalysts. To achieve this target, two strategies are suggested in current studies, namely the graded distributions of Pt loading inside the CL and the electrode porosity within the GDL [7]. Optimal arranged distribution of Pt loading can better match the electrochemical reaction and mass transport, leading to improved catalytic efficiency. Due to the spatial variation of reactant concentration within the porous electrode at different operating conditions, appropriately changing Pt loading according to the reaction situation can reduce the usage and improve the utilisation of Pt catalysts [10, 11]. On the other hand, the effective mass transport rates of reactants, water, electrons, and heat are alerted by GDL porosity according to the Bruggeman correlation [12]. For instants, mass, electron, and heat transfer were found to be significantly affected by GDL porosity [13, 14]. Therefore, we propose to develop a model to simultaneously investigate the cell performance and uniformity of current distribution of a PEMFC operated with graded Pt loading and GDL porosity, intending to improve the cell performance and generate homogenously distributed current density over the entire electrode.

The graded design of Pt loading and GDL porosity can be classified into through-plane and in-plane directions. The through-plane graded design is to change the Pt loading and GDL porosity through the electrode thickness, which is the reactant diffusion direction. On the contrary, the in-plane graded design is the variation of Pt loading and GDL porosity from the inlet to the outlet along the reactant flow direction. Antoine et al. [15] studied the change of catalytic efficiency of Pt loading under porous and non-porous active layers conditions with gradient change. Porous and non-porous Pt loading have higher catalytic efficiency near the membrane with higher current density. Taylor et al. [16] used inkjet printing technology to prepare a similar inhomogeneous CL, and this structure also improved the cell performance compared with traditional PEMFC. Matsuda et al. [17] designed a multi-CL layer structure to observe the changes in PEMFC performance by changing humidity in the CL. The results showed that under the condition of relatively high humidity, the partial pressure of oxygen near GDL decreased significantly, and the Pt loading should be increased to convert more oxygen. Kongstein et al.

[18] designed a multi-layer CL with higher Pt loading near the membrane (50 wt% Pt/C) than that far away from the membrane (20 wt% Pt/C). This multi-layer CL achieved the maximum energy density of 0.83W/cm^2 at 0.4 V. Su et al. [19] designed a multi-layer CL structure with polytetrafluoroethylene (PTFE) near the membrane side and polyvinylidene fluoride (PVDF) close to the gas channel. The results showed that the Pt content of PVDF had a significant effect on the electrode dynamics, and the mass transfer was mainly affected by the platinum content of PTFE. This structure design significantly improved the performance and service life of PEMFCs. Roshandel and Ahmadi [20] concluded that a higher reaction rate region should have higher Pt loading to increase the current density and power density. For the distribution of Pt loading, this study area comes with some controversy, for instance, Srinivasarao et al. [21] suggest increasing Pt concentration near the membrane side can effectively improve the performance of PEMFC, this faction mainly considers the impact of water which reduce the gas transfer. but most experimental studies proved near the membrane side with high Pt loading could achieve better performance. [15-17] The improvement of PEMFC performance is mainly concentrated in the area with middle or high current density. Theoretically, high Pt concentration near the GDL side more easily achieves high performance, because placing more catalysts in the area with the highest oxygen concentration could achieve the highest reaction rate, then increases the cell performance. However, this is only the theoretical result due to the ionomer network not necessarily being continuous, which generates elevated resistance for proton transport via the ionomer network. In this study, a homogeneous ionomer network has been assumed. Owing to the appropriately reduced Pt loading within different layers of the multi-layer CL design, the catalytic efficiency of different layers could be properly matched, and the usage of Pt is reduced. Along the in-plane direction, Prasanna et al. [22] proved that the graded distribution of Pt along the reactant flow direction improved both the cell performance and catalyst utilization in the high current density range. Xing et al.'s study [23] revealed that the in-plane variation of Pt loading, incorporated with graded GDL porosity, could achieve a more uniform current density and reduce the use of Pt.

In addition to the graded Pt loading distribution within the CL, the graded design of GDL

porosity is also important owing to the influence on the effective diffusion coefficient of reactant gases. Reasonable distribution of GDL porosity could better manage reactant mass transport and water removal, and then improve the cell performance [24-27]. Chu et al. [28] reported the effect of different sized GDL pores on oxygen mass distribution, membrane phase potential and current density in non-uniform pores of PEMFCs. The results showed that the current density increases when the GDL porosity increases, and this result was proven by Roshandel et al. [29]. The model developed by Chen et al. [30] studied the graded GDL porosity along the through-plane direction and detected the molar concentration changes of water and oxygen. The results showed that the gradient pore design was beneficial to reduce the water accumulation, increase the effective porosity in GDL, and improved the PEMFC performance. The three-dimensional model designed by Huang et al. [31] also proved that high GDL porosity away from CL and low porosity near CL can effectively improve the current density by 17.73% when the optimal distribution strategy was used. Zhan et al. [32] showed that a large gradient of GDL porosity benefits gas diffusion and water discharge. Zhang et al. [33] used exponential function to study the change of porosity gradient and verified this design through experiments after corresponding optimisation. The results showed that the exponential change of GDL porosity achieved a more uniform current density and higher power density. Concerning the in-plane direction, Lim et al. [34] indicated that, compared with non-gradient change PEMFC, GDL with in-plane gradient change improved 9% in the cell performance and uniformized 4% in the current distribution. Wang et al. [35] proved that the in-plane direction gradient change enhances the mass transfer and the ability of water removal.

The graded distributions of Pt loading and GDL porosity could improve the cell performance and achieve a more uniform current distribution of PEMFCs. Most previous work only focused on the variation of Pt loading or GDL porosity along a single direction, either through-plane or in-plane direction. For practical PEMFCs, it is more insightful to consider both through-plane and in-plane situations with the graded design of multi-variables. However, due to huge design space, limitation of conventional method, Machine learning (ML) algorithm – one of the major artificial intelligence (AI) applications is used for our research to significantly save

computational resource and time. The algorithm establishes the connection between inputs and outputs based on the principle of statistics. The commonly used ML algorithms mainly include artificial neural network (ANN), support vector machine (SVM) et al [36]. These algorithms are generally used in cell performance prediction, life prediction and material optimization of PEMFCs [37-39]. The evaluation criterion of the algorithms is accuracy. Mehrpooya et al. [37] used the Group Method of Data Handling – Genetic algorithms (GMDH-GA) neural network to explore the internal relationship between temperature, humidity, oxygen, hydrogen flow rate and the PEMFC performance. The accuracy of the training set and test set were 0.982 and 0.9723 respectively. Han and Chung [38] compared the PEMFC performance of using ANN and SVM algorithms with variables of temperature, humidity, and pressure as inputs. The results showed that the ANN's accuracy is 0.9995 and the maximum mean absolute percentage error is 0.2%, which is better than that of SVM (0.982 with the maximum mean absolute percentage error of 0.88%). However, the ANN algorithm may be less accurate than SVM, as to the influence of the database. For example, the results of SVM in Kheirandish et al.'s study [40-42] were better than those of ANN. Wang et al.'s study [43] pointed out that different physical fields will produce different predictive performances when using the same algorithm. All the above shows that the ML algorithm has emerged in PEMFC research. ANN is chosen as the main method to study according to its strong adaptability and accuracy of data processing.

However, these studies still have some deficiencies during the studies of inhomogeneous Pt loading and GDL porosity, for instance: 1). the variation of Pt loading along the through-plane direction is not salient compared with that along the in-plane direction; 2). the gradient change of porosity is dominated by a single direction, and the effect of simultaneous changes in two directions on the current density is not considered: 3). lack of comprehensive studies of the interaction of Pt loading and GDL porosity; and 4). the time-consuming and computing resources dependent simulation. The objective of this study is to reveal the impact of multi gradient change in Pt loading and GDL porosity to current density, and ultimately propose using ML algorithms to assist the process of simulation, which can benefit the PEMFC design while maintaining a relatively low cost and high accuracy.

2. Model development and validation

2.1 Model development

A two-dimensional, along-the-channel, multi-physics, two-phase flow, non-isothermal model was developed based on the geometry as shown in Fig. 1. The modelling domain consists of two gas diffusion layers (GDLs), two catalyst layers (CLs) and a proton exchange membrane (PEM) sandwiched in between.

The main assumptions are given as follows:

1. The feed gases are treated as ideal gases.

2. CLs are constructed of Pt/C agglomerates in turn covered by ionomer and liquid water films [44].

3. PEM is impermeable to hydrogen, oxygen, and nitrogen.

4. The deformation of PEM, GDLs and CLs under clamping force is neglected.

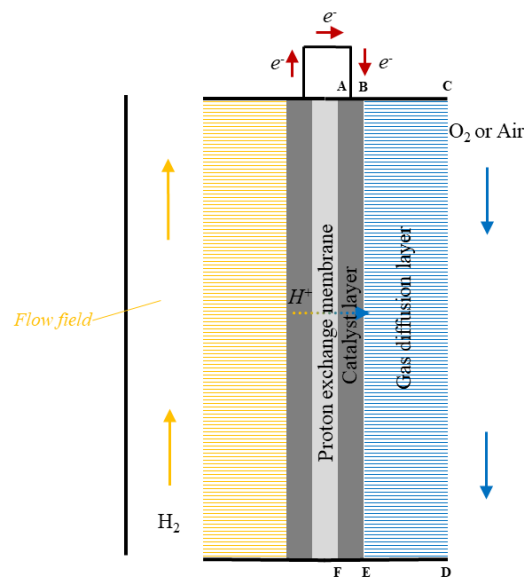5. The contact resistance between each component is neglected.

Figure 1 2D along-the-channel sketch of a PEM fuel cell and the modelling domain, point A is $m_{Pt,0}$, point B indicates $m_{Pt,1}$ and $\varepsilon_{GDL,0}$, point C represents $\varepsilon_{GDL,1}$, point D refer to $\varepsilon_{GDL,3}$, point E delegates $m_{Pt,3}$ and $\varepsilon_{GDL,2}$, point F is $m_{Pt,2}$.

2.2 Governing equation

2.2.1 Conservation of species

The mass transport of gas species in porous media is described by the Maxwell-Stefan equation as follows [23]:

$$\rho_g u_g \nabla w_i - \nabla \cdot [\rho_g \sum_j D_{ij}^{eff} (\nabla x_j - x_j) \frac{\nabla p}{p}] = M_i S_i \tag{1}$$

where p is the pressure, ρ_g and u_g are the density and velocity of gas mixture, w_i, x_i, and M_i represent mass fraction, mole fraction, molecular weight of species i, respectively, effective diffusion coefficient, respectively. S_i is the source term of different gaseous species, i.e., hydrogen, oxygen and vapour, which could be found elsewhere [23]. The effective diffusion coefficient in the porous media, D_{ij}^{eff}, is calculated by the following equation based on the Bruggeman formula:

$$D_{ij}^{eff} = [(1-s)\varepsilon]^{1.5} \cdot D_{ij} \tag{2}$$

where the subscript i and j represent gas species, ε represents the initial porosity of the porous media, D_{ij} is the Maxwell-Stefan diffusion coefficient matrix, s is the water saturation, representing the volume fraction of void space of the porous media occupied by liquid water.

2.2.2 Conservation of momentum

The velocity of the reactant gases, u_g, in porous media is expressed by the continuity equation and Navier-Stokes equation:

$$\nabla \cdot (\rho_g u_g) = S_m \tag{3}$$

$$\frac{\rho_g}{\varepsilon^2}(u_g \cdot \nabla u_g) = -\nabla p - \frac{\mu_g}{\varepsilon}\left[\nabla u_g + (\nabla u_g)^T - \frac{2}{3\varepsilon}(\nabla \cdot u_g)I\right] - (\frac{\mu_g}{k_p})u_g \tag{4}$$

where $u_g \cdot \nabla u_g$ is convective acceleration, ∇p is pressure gradient, μ^g is the viscosity of the gas mixture, I is the identity matrix, ε and k_p are the porosity and permeability of the porous media, respectively. S_m is the source term of gas mixture, accounting for the sum of individual source term of hydrogen, oxygen and vapor. Details could be found elsewhere [45].

2.2.3 Conservation of charge

The conservation of charge at the anode and cathode can be expressed as the following equations:

$$\nabla i_s + \nabla i_l = 0 \tag{5}$$

$$i_s = -\sigma_s^{eff} \nabla \phi_s \tag{6}$$

$$i_l = -\sigma_l^{eff} \nabla \phi_l \tag{7}$$

where σ_s and σ_l are the effective conductivity of the electrode and electrolyte, i_s and i_l are the current density of the electrode and electrolyte, respectively.

The electrochemical reaction rate of the HOR and the ORR can be calculated by the following equations based on the Bulter-Volmer kinetic equation and spherical agglomerate assumption [44, 46]:

$$i_a = a_{agg} i_{0,a}^{ref} (\frac{p_{H_2}}{H_{H_2} c_{H_2}^{ref}})^{0.5} \left\{ \exp(\frac{\alpha_a F \eta_a}{RT}) - \exp[-\frac{(1-\alpha_a)F\eta_a}{RT}] \right\} \tag{8}$$

$$i_c = 4F \frac{p_{H_2}}{H_{H_2}} \left[\frac{1}{E_{agg} k_{agg}} + \frac{r_{agg} + \delta_{ele} + \delta_w}{r_{agg}} (\frac{\delta_{ele}}{a_{agg} D_{O_2-ele}^{eff}} + \frac{\delta_w}{a_{agg} D_{O_2-w}^{eff}}) \right]^{-1} \tag{9}$$

where p_i and H_i are the partial pressure of reactant gases and Henry's constant at the anode and cathode, respectively. a_{agg} is the effective specific area of the catalyst layer, c_{H2}^{ref} represents the reference hydrogen mole concentration, $i_{0,a}^{ref}$ is the anode exchange current density, r_{agg} is the radius of agglomerate, δ_{ele} and δ_w represent the total thickness of the ionomer film and liquid water film, respectively. E_{agg} is an effectiveness factor of the spherical agglomerate which can be expressed as [44, 47-49]:

$$E_{agg} = \frac{1}{M_{T,agg}} [\frac{1}{\tanh(3M_{T,agg})} - \frac{1}{3M_{T,agg}}] \tag{10}$$

where $M_{T,agg}$ is a dimensionless parameter named Thiele' modulus, which can be calculated using the equation [44, 50]:

$$M_{T,agg} = \frac{r_{agg}}{3} \sqrt{\frac{k_{agg}}{D_{O_2-p}^{eff}}} \tag{11}$$

10

where $D_{O_2-p}^{eff}$ is the effective diffusion coefficient of oxygen through the void space and k_{agg} is the reaction rate coefficient of the cathode, which is expressed as

$$k_{agg} = \frac{a_{agg} i_{0,c}^{ref}}{4Fc_{O_2}^{ref}} \left\{ \exp(\frac{-\alpha_c F \eta_c}{RT}) - \exp[\frac{(1-\alpha_c)F\eta_c}{RT}] \right\} \qquad (12)$$

where c_{O2}^{ref} is the reference oxygen concentration, $i_{0,c}^{ref}$ is the cathode reference exchange current density, α_c is the charge transfer coefficient and η_c is the overpotential of the cathode, expressed as follows:

$$\eta_c = \phi_{s,c} - \phi_{l,c} - E_c^{eq} \qquad (13)$$

where $\phi_{s,c}$, $\phi_{l,c}$ and E_c^{eq} are the potentials of the solid phase, electrolyte phase and the equilibrium potential of the cathode, respectively. The equilibrium potential of the anode is zero.

2.2.4 Transport of liquid water in porous media

The governing equation of the liquid water transport in the porous medium is derived from Darcy's law based on the volume of fluid (VOF) approach. At steady-state conditions, it can be expressed as follows [46, 51]:

$$\rho_w D_c \nabla^2 s - \frac{\rho_w k_r^l \mu_w^g}{k_r^g \mu_w^l} \nabla u_g = M_w S_w^l \qquad (14)$$

where ρ_w and M_w are the density and molecular weight of liquid water, respectively, μ_w^g and μ_w^l are the viscosity of water vapour and liquid water, k_r^g and k_r^l are the relative permeability of gas and liquid phase, respectively. S_w^l is the source term of liquid water, details could be found elsewhere [52].

The capillary diffusion coefficient, D_c, is calculated using the following equation [53]:

$$D_c = -\frac{k_r^l}{\mu_w^l} \sigma_w \cos(\theta_c)(\varepsilon k_p)^{1/2} \frac{dJ(s)}{ds} \qquad (15)$$

where σ_w is the surface tension of liquid water, θ_c is the contact angle, k_p is the permeability of the electrode, and $J(s)$ is the Leveret J-function, expressed as [54, 55]

$$J(s) = \begin{cases} 1.417(1-s) - 2.120(1-s)^2 + 1.263(1-s)^3 & \theta_c \leq 90° \\ 1.417s - 2.120s^2 + 1.263s^3 & \theta_c < 90° \end{cases} \qquad (16)$$

2.2.5 Transport of dissolved water through the membrane

Dissolved water transport through the membrane consists of three mechanisms: electro-osmotic drag (EOD), back diffusion and hydraulic permeation. In our model, a second-order partial differential equation is developed to describe this process [45]:

$$\nabla \cdot (n_d \frac{i_m}{F}) - \nabla \cdot (D_w^m \nabla c_w^d) - \nabla \cdot (\frac{k_p^m c_w^d}{\mu_w^l} \nabla p) = S_w^d \qquad (17)$$

where n_d represents the EOD coefficient, which is expressed as $2.5\lambda/22$, i_m is the electrolyte current density, F is the Faraday's constant, k_p^m is the membrane permeability, D_w^m is the diffusivity of the dissolved water through the membrane. S_w^d is the source term of dissolved water, details could be found elsewhere [51]. The concentration of the dissolved water, c_w^d, is a function of the water content of the membrane and ionomer, as follows:

$$c_w^d = \frac{\rho_m}{EW} \frac{\lambda}{1 + k_s \lambda} \qquad (18)$$

where ρ_m and EW are the density and equivalent weight of dry membrane, k_s is the swelling coefficient, which is used to describe the volume increase of the membrane and ionomer. The water content, λ, is described as a function of water activity [54]:

$$\lambda = \begin{cases} 0.043 + 17.81\alpha_w - 39.85\alpha_w^2 + 36.0\alpha_w^3 & \alpha_w < 1 \\ 14.0 + 1.4(\alpha_w - 1) & 1 \le \alpha_w \le 3 \\ 16.8 & \alpha_w > 3 \end{cases} \qquad (19)$$

$$\alpha_w = x_w p / p_w^{sat} + 2s \qquad (20)$$

where p is the operating pressure, p_w^{sat} represents the saturation pressure of vapour, as a function of temperature, expressed as

$$p_w^{sat} = 9.531 \times 10^{-4}(T - 237)^4 - 3.123 \times 10^{-2}(T - 237)^3 + 3.451(T - 237)^2 + 20.96(T - 237) + 611.0 \qquad (21)$$

2.2.6 Electrode properties

The CLs consist of platinum, carbon, the ionomer, void space, and a portion of GDL remained in the CL. Assuming CL uniformly intrudes into GDL, the sum of the volume fractions of the components is equal to unity.

$$L_{Pt} + L_C + L_{ele} + \varepsilon_{CL} + L_S = 1 \tag{22}$$

The volume fractions of Pt, carbon black, the ionomer, and GDL penetration can be expressed as follows:

$$L_{Pt} = \frac{m_{Pt}}{\rho_{Pt} l_{CL}}, \; L_C = \frac{m_C}{\rho_C l_{CL}}, \; L_{ele} = \frac{m_{ele}}{\rho_{ele} l_{CL}} \; L_S = L_{GDL}(1 - \varepsilon_{GDL}) \tag{23}$$

where, m_{Pt}, m_C and m_{ele} are the mass loadings of platinum, carbon, and the ionomer; ρ_{Pt}, ρ_C, and ρ_{ele} are the densities of platinum, carbon, and the ionomer, respectively. l_{CL} is the CL thickness, ε_{GDL} is the GDL porosity, and L_{GDL} is the volume fraction of the GDL remained in the CL. Platinum is normally well dispersed in carbon black to prepare carbon-dispersed platinum (Pt/C). Therefore, the volume fraction of Pt/C is the sum of the volume fractions of Pt and C, which is given as follows:

$$L_{Pt/C} = \frac{m_{Pt}}{l_{CL}} \left(\frac{1}{\rho_{Pt}} + \frac{1-f}{f} \frac{1}{\rho_C} \right) \tag{24}$$

where the platinum mass ratio to that of carbon (abbreviated as the platinum mass ratio) is expressed as [44]

$$f = \frac{m_{Pt}}{m_{Pt} + m_C} \tag{25}$$

By combining Eq. (22) - (25), the porosity of the CL is calculated by [44]

$$\varepsilon_{CL} = 1 - L_{ele} - L_S - \frac{m_{Pt}}{l_{CL}} \left(\frac{1}{\rho_{Pt}} + \frac{1-f}{f} \frac{1}{\rho_C} \right) \tag{26}$$

The agglomerate density, defined as the number of agglomerates in a fixed volume of CL, is calculated by [56, 57]:

$$N_{agg} = \frac{3L_{Pt/C}}{4(1-\varepsilon_{CL})\pi r_{agg}^3} \tag{27}$$

The specific area of the agglomerate is expressed as [56, 57]

$$a_{agg} = \frac{m_{Pt} A_s}{l_{CL}} \frac{(1-\varepsilon_{CL})}{L_{Pt/C}} \tag{28}$$

where A_s is the reaction surface area per unit platinum mass, which is expressed as [58]

$$A_s = (227.79 f^3 - 158.57 f^2 - 201.53 f + 159.5) \times 10^3 \tag{29}$$

The effective GDL conductivity is a function of its porosity, which could be expressed by the Burgmann correlation as follow:

$$\sigma_{GDL}^{eff} = (1 - \varepsilon_{GDL})^{1.5} \sigma_{GDL}^0 \tag{30}$$

where ε_{GDL} is the GDL porosity and σ_{GDL}^0 is the intrinsic conductivity, respectively.

The effective CL conductivity is determined by its compositions, which could be calculated by

$$\sigma_{CL}^{eff} = \sigma_{Pt} L_{Pt}^{1.5} + \sigma_C L_C^{1.5} \tag{31}$$

Different from uniform distributions of Pt loading and GDL porosity in previous work, we designed a graded distribution of Pt loading and GDL porosity in two directions, namely the through-plane reactant gas diffusion direction (x direction) and the in-plane gas flow direction from the inlet to outlet of the cathode (y direction). The distribution functions of the two studied parameters are given as follows:

$$m_{Pt,c} = m_{Pt,0} + k_{Pt,x} \frac{x^2}{\delta_{CL}} + k_{Pt,y} \frac{(L_{ch} - y)^2}{L_{ch}} \tag{32}$$

$$\varepsilon_{GDL,c} = \varepsilon_{GDL,0} + k_{GDL,x} \frac{x^2}{\delta_{GDL}} + k_{GDL,y} \frac{(L_{ch} - y)^2}{L_{ch}} \tag{33}$$

where $m_{Pt,0}$ is the Pt loading at the PEM-CL interface at the cathode inlet, $\varepsilon_{GDL,0}$ is the GDL porosity at the CL-GDL interface at the cathode inlet, L_{ch} is the length of the channel, δ_{GDL} and δ_{CL} are the thickness of the CL and GDL, respectively. Pt loading within the CL and porosity of the GDL are designed to obey linear distribution, and the gradients of Pt loading and porosity are expressed as

$$k_{Pt,x} = (m_{Pt,1} - m_{Pt,0}) / \delta_{CL} \ , \ k_{Pt,y} = (m_{Pt,2} - m_{Pt,0}) / L_{ch} \tag{34}$$

$$k_{GDL,x} = (\varepsilon_{GDL,1} - \varepsilon_{GDL,0}) / \delta_{GDL} \ , \ k_{GDL,y} = (\varepsilon_{GDL,2} - \varepsilon_{GDL,0}) / L_{ch} \tag{35}$$

where $m_{Pt,1}$ is the Pt loadings at the CL-GDL interface at the cathode inlet, $m_{Pt,2}$ is the Pt loading at the CL-membrane interface at the cathode outlet, $\varepsilon_{GDL,1}$ is the GDL porosity at the GDL-
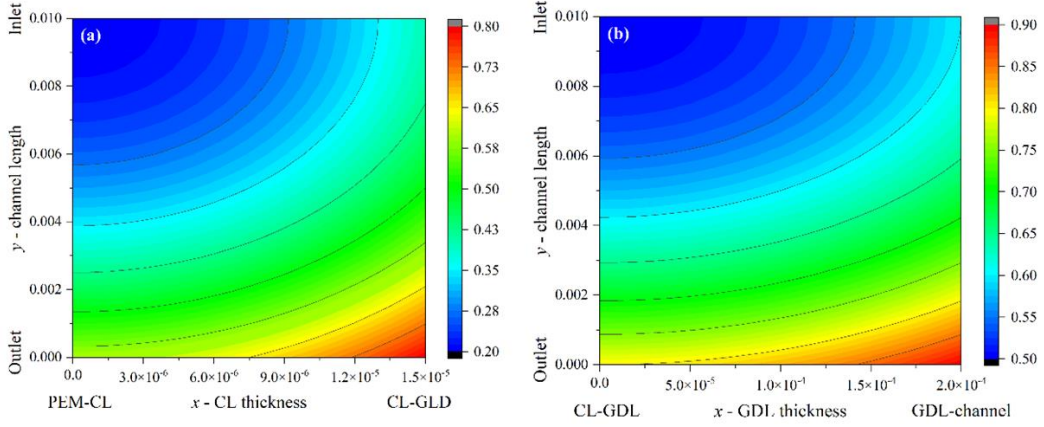
Figure 2 Profiles of Pt loading (a) and GDL porosity (b) with $m_{Pt,0} = 0.2$ mg cm^{-2}, $m_{Pt,1} = 0.4$ mg cm^{-2}, $m_{Pt,2} = 0.6$ mg cm^{-2}; and $\varepsilon_{GDL,0} = 0.5$, $\varepsilon_{GDL,1} = 0.6$, $\varepsilon_{GDL,2} = 0.8$.

channel interface at the cathode inlet, and $\varepsilon_{GDL,2}$ is the GDL porosity at the CL-GDL interface

at the cathode outlet, respectively.

At the cathode outlet, the Pt loading at the CL-GDL interface, $m_{Pt,3}$, and GDL porosity at the

GDL-channel interface, $\varepsilon_{GDL,3}$, are calculated by the following expressions:

$$m_{Pt,3} = m_{Pt,1} + m_{Pt,2} - m_{Pt,0} \tag{36}$$

$$\varepsilon_{GDL,3} = \varepsilon_{GDL,1} + \varepsilon_{GDL,2} - \varepsilon_{GDL,0} \tag{37}$$

It is known from the above expressions that the maximum Pt loading and GDL porosity could

be constrained within the corresponding computational domains. In this work, the maximum Pt

loading and GDL porosity are controlled to 0.9 mg cm^{-2} and 0.9, respectively. Fig.2 is one

example that distribution of Pt laoding and and GDL porosity. This example stricted by Eq.

(32)-(37).

The average Pt loading and GDL porosity could be calculated through the integration of Eq.

(31) and (32), leading to the following expressions:

$$m_{Pt,c}^{ave} = \frac{\int_0^{L_{ch}} \int_0^{\delta_{CL}} m_{Pt,c} dx dy}{L_{ch} \cdot \delta_{CL}} = \frac{m_{pt,0} + m_{pt,1} + m_{pt,2}}{3} \tag{38}$$

$$\varepsilon_{GDL,c}^{ave} = \frac{\int_0^{L_{ch}} \int_0^{\delta_{GDL}} \varepsilon_{GDL,c} dx dy}{L_{ch} \cdot \delta_{GDL}} = \frac{\varepsilon_{GDL,0} + \varepsilon_{GDL,1} + \varepsilon_{GDL,2}}{3} \tag{39}$$

The homogeneity of current distribution is evaluated by the coefficient of variation, which is

expressed by the following equation:

$$S = \sqrt{\frac{\sum_{i=1}^{n}(x_i - \bar{x})^2}{n-1}} \bigg/ \bar{x} \qquad (40)$$

where n is the number of point in the CL, $\bar{x}$ indicates the average of current density, x_i is the current density at current point. The range of S is [0,1], the smaller value indicates the higher uniformity of current density profile over the CL.

2.3 Boundary conditions

Table 1 is the parameters used in the model in base-case condition. The boundary conditions, e. g. operating temperature, mole fractions of reactant gases, pressure, gas velocities and liquid water saturation, at the inlets of the anode and cathodes, are defined as follows:

Table 1 Parameters used in the model in base-case condition

Symbol(unit)	Description	Value	Reference
L_{ch} (mm)	Channel length	10	measured
δ_{Ch} (mm)	Channel depth	1	measured
δ_{GDL} (μm)	GDL thickness	300	measured
δ_{CL} (μm)	CL thickness	15	measured
δ_M (μm)	PEM thickness	55	measured
ε_{GDL}	GDL porosity	Eq. (33)	calculated
ε_{CL}	CL porosity	Eq. (26)	calculated
m_{Pt}	Platinum loading (mg cm^{-2})	Eq. (32)	calculated
f	Platinum mass ratio	40%	measured
m_M	Ionomer loading (mg cm^{-2})	0.4	measured
σ_{GDL} (S m^{-1})	GDL conductivity (S m^{-1})	Eq. (30)	calculated
σ_{CL} (S m^{-1})	CL conductivity (S m^{-1})	Eq. (31)	calculated
T (K)	Operating temperature (K)	298.15	measured
p	Operating pressure (atm)	1.0	measured
RH	Relative humidity	100%	measured
α_a	Anode charge-transfer coefficient	0.5	[47]
α_c	Cathode charge-transfer coefficient	0.7	[47]
r_{agg} (μm)	Agglomerate radius	0.1	[23]
ξ_a	Anode stoichiometry	1.0	measured
ξ_c	Cathode stoichiometry	2.0	measured

$$T_a = T^0, \ p_a = p_a^0, \ s_a = 0, \ x_{w,a}^0 = p_w^{sat} RH_a / p_a, \ x_{H_2}^0 = 1 - x_{w,a}^0 \tag{41}$$

$$T_c = T^0, \ p_c = p_c^0, \ s_c = 0, \ x_{w,c}^0 = p_w^{sat} RH_c / p_c, \ x_{O_2}^0 = 0.21(1 - x_{w,c}^0), \ x_{N_2}^0 = 0.79(1 - x_{w,c}^0)$$
$$\tag{42}$$

$$u_{g,a}^0 = \frac{\xi_a RT i^{ref} A_M}{2 F p_a x_{H_2} A_{ch}}, \ u_{g,c}^0 = \frac{\xi_c RT i^{ref} A_M}{4 F p_c x_{O_2} A_{ch}} \tag{43}$$

where i^{ref} is the reference current density, ξ_a and ξ_c are the stoichiometric flow ratios of the anode and the cathode, respectively. A_M and A_{ch} are the effective area of the electrode and the cross-sectional area of the channel, respectively. The inlet pressure (p_a^0 and p_c^0), relative humidity (RH_a^0 and RH_c^0), liquid water saturation (s) and operating temperature (T) at the inlets of the anode and cathode are set as 1 atm, 100%, zero and 70 °C, respectively.

The water content at the CL-GDL interface of the anode and cathode are defined as the Dirichlet boundaries, which are expressed by the following equation:

$$\lambda^0 = 0.043 + 17.81\alpha_w - 39.85\alpha_w^2 + 36.0\alpha_w^3 \tag{44}$$

where α_w is the water activity, which could be calculated by Eq. (19) based on the values of relevant parameters at inlet conditions.

2.4 Numerical procedure

Commercial software, COMSOL Multiphysics, is used to solve the fully coupled equations in the mathematical model. The polarisation curve is obtained by setting the cell voltage as a boundary condition and computing the current density through an iteration process, which is repeated until the calculation error is lower than 1×10^{-6}. The parameter sweep method is used for the studied cell voltage varying from 1.1 to 0.1 V.

2.5 AI modelling

In this work, a current density at a given low cell voltage, i.e., 0.1 V, is chosen for characterisation, which is influenced by multiple variables, e.g., material properties, cell design, experimental conditions, and electrochemical/physical processes. The variations of Pt loading and GDL porosity at different corners of the computational domain construct six inputs of the data-driven model. The current density at 0.1 V is selected as the output label. Sampling data

is generated by solving the physics based mechanistic PEMFC model through COMSOL. After

data points screening through the Latin hypercube algorithm, they are applied for training the

data-driven model based on the recurrent neural network (RNN) algorithm. The potential of the

RNN algorithm has recently been rediscovered due to its unique feature of internal memory,

which can establish effective relations between input sequence data. For a limited range of

outputs, the increments Δ between adjacent data may be linearly dependent because the

expected result is continuous in the database.

In this study, RNN-LSTM was chosen to process the permutation and combination of six

parameters, with 9^6 combination possibilities, while the accuracy of the parameter is 0.1.

Furthermore, the studied database is a sparse matrix with around 5,000 data, which is restricted

by Eq. (32) – (37). Moreover, the memory cell of RNN is unique, which could process the

sparse matrix with continuity in the data, and LSTM enhances this function in the algorithm.

In RNN, for each timestep t, the relation between activation $a^{<t>}$ and output $y^{<t>}$ are [59]:

$$a^{<t>} = g_1(W_{aa}a^{<t-1>} + W_{ax}x^{<t>} + b_a), y^{<t>} = g_2(W_{ya}a^{<t>} + b_y) \qquad (45)$$

where W_{aa}, W_{ax}, W_{ya} could recognize as weight in the node aa, ax, ya briefly; b_a and b_y are

the offset, g_1 and g_2 are activation functions.

The most common activation functions are Sigmoid[59]:

$$g(z) = \frac{1}{1 + e^{-z}} \qquad (46)$$

And Tanh[59]:

$$g(z) = \frac{e^z - e^{-z}}{e^z + e^{-z}} \qquad (47)$$

Loss function $\mathcal{L}$ is[59]:

$$L(\hat{y}, y) = \sum_{t=1}^{Ty} L(\hat{y}^{<t>}, y^{<t>}) \qquad (48)$$

where T is timestep. The loss L and weigh matrix W form the backpropagation function[59]:

$$\frac{\partial L^{<T>}}{\partial W} = \sum_{t=1}^{T} \frac{\partial L^{<T>}}{\partial W}\Big|_{(t)} \qquad (49)$$

After the Latin hypercube sampling method is used to sample data, the preset value of unselected points is 0, and the distribution of sampling points in the sampling space is a sparse matrix. According to the description and definition, RNN can only remember short-term memory, that is, data with short steps. Due to the characteristics of the sparse matrix, we also need to use long and short-term memory (LSTM) algorithm to improve RNN.

The LSTM algorithm consists of three gates, and the forget gate algorithm is[59]:

$$f_t = \sigma_g(W_f x_t + U_f h_{t-1} + b_f) \tag{50}$$

where σ_g is sigmoid active function, x_t is input, W_f, U_f, b_f are weights and biases, h_{t-1} is the output of the previous phase. This function control if forget.

The output gate is composed of two algorithms[59]:

$$i_t = \sigma_g(W_i x_t + U_i h_{t-1} + b_i) \tag{51}$$

$$a_t = \tanh(W_a x_t + U_a h_{t-1} + b_a) \tag{52}$$

Before getting the output gate, the computing part – cell c_t also needs to update[59]:

$$c_t = c_{t-1} \odot f_c + i_t \odot a_t \tag{53}$$

where $\odot$ is Hadamard product. The output gate o_t is[59]:

$$o_t = \sigma_g(W_o x_t + U_o h_{t-1} + b_o) \tag{54}$$

$$h_t = o_t \odot \tanh(c_t) \tag{55}$$

2.6 Model validation

Model validation is presented in Fig. 4, in which the modelling results of homogeneous distributions of Pt loading and GDL porosity are compared with both in-house experimental data and the experimental results from the literature of Wang et al. [60] respectively. The fuel cell properties and operating conditions for model validation are listed in Table 2.
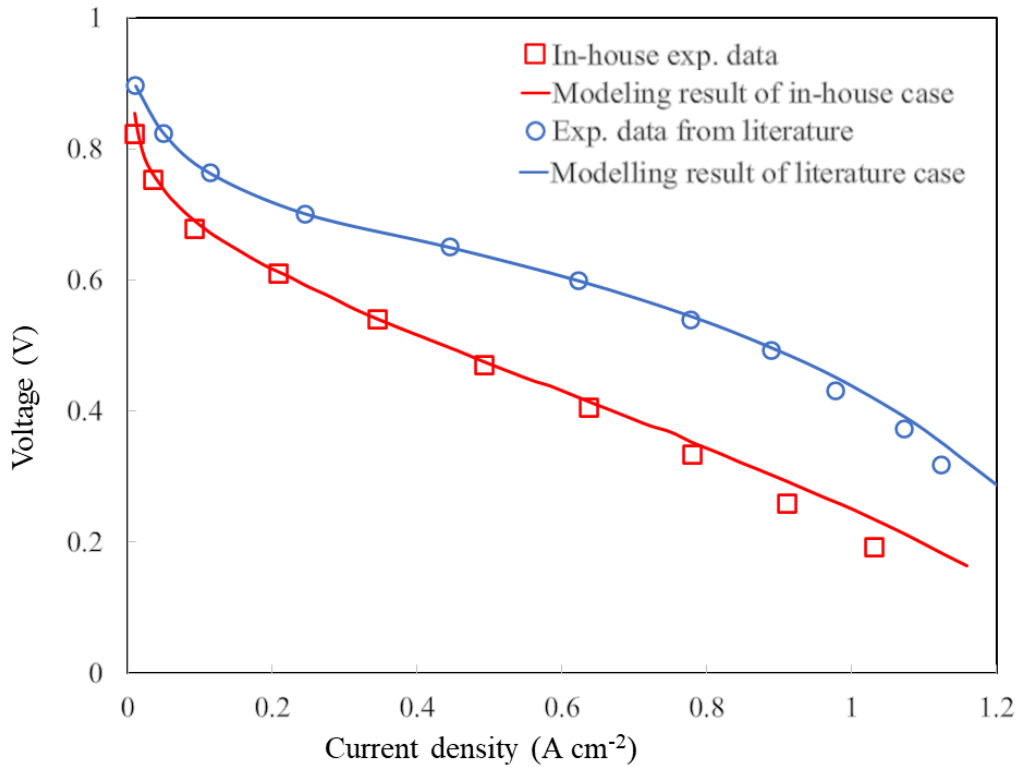
Figure 3 Model validation

Both modelling results agree well with the experimental data in low and media current density ranges. The discrepancy of modelling and experimental results at high current densities could be explained by the severe water formation and accumulation along the channel. In the work of Wang et al. [60], a longer serpentine channel was used in the experimental measurement, leading to a higher amount of liquid water than the shorter parallel channel used in the model. In short, the good consistency of modelling and experimental results at low and medium current densities prove the correctness and accuracy of the model.
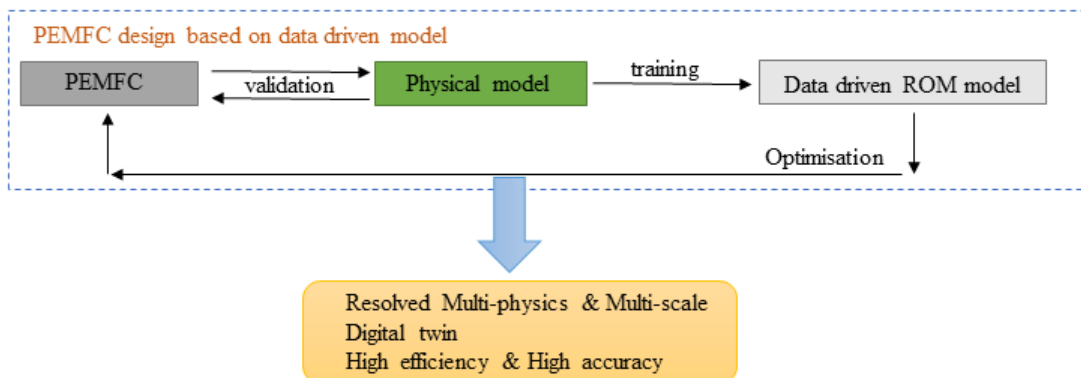

Figure 4 Process of data-driven model

Table 2 Parameters used for model validation

Symbol	Description(unit)	Validation In-house	Validation Literature
L_{Ch} (mm)	Channel length	10	70
δ_{Ch} (mm)	Channel depth	1.0	1.0
δ_{GDL} (μm)	GDL thickness	300	300
l_{CL} (μm)	CL thickness	15	15
l_M (μm)	PEM thickness	55	108
ε_{GDL}	GDL porosity	0.4	0.4
m_{Pt}^0 (mg cm^{-2})	Platinum loading	0.4	0.4
f	Platinum mass ratio	20%	40%
m_M^0 (mg cm^{-2})	Ionomer loading	0.4	1.0
α_C	Cathode charge transfer coefficient	0.85	0.85
T (K)	Operation temperature	333	343
p (atm)	Back Pressure	1.0	1.0
RH	Relative humidity	100%	100%
ξ_a	Anode stoichiometry	11.8[a]	1.0[b]
ξ_c	Cathode stoichiometry	12.4[a]	1.4[b]

[a] Calculated at the volumetric flow ratio of 200 and 500 sccm using Eq. (43) for anode and cathode, respectively, at operation conditions.

[b] Calculated at the volumetric flow ratio of 1200 and 2200 sccm using Eq. (43) for anode and cathode, respectively, at given operation conditions in Wang et al.[60]

In the ML process, the output label tag is set as the current density (the indicator of performance) and its coefficient of variation (the indicator of homogeneity). Both R^2 and RMSE are used as indicators to evaluate two objective functions in the output tag, owing to the probably weak linear relationship between the input and output label. It is generally accepted that R^2 has better performance to descript the linear relationship, but RMSE has a better adaptation in the non-linear database. All those conclusions have been proved in the research of Spiess et al. [61] and Abdi et al. [62]. The process of this study is summarised in Fig. 4.

2.7 Evaluation of data-driven surrogate model

In Fig. 1, six parameters are permutations and combinations under the restriction of Eq. (32), (33), (36) and (37). It obtains about 5000 nodes. Nodes are unequally distributed because the number of nodes with small values at point A (for Pt loading) or point B (for GDL porosity) are significantly greater than the number of nodes with large values. The Latin hypercube sampling method is used to combine the sampling of nodes to ensure that the proportion of sampling points in the segmented region is the same. After the initial value is obtained through solving the mechanistic PEMFC model, the obtained data can contain as many features of the 5000 nodes as possible.

The filtered data is divided into a set of training and test. The training set is used to train the algorithm, and the test set is used to test whether the algorithm obtained by training is reliable. R^2 and RMSE are used as indicators to evaluate the accuracy of the data-driven model. In addition, the unselected data will be used as the prediction set, and the algorithm with high accuracy will be used to predict after the training is completed.

3. Results and discussion

The simulation results have been categorised into two groups for single-variable and dual-variable studies. The single-variable group follows the single variable change, as to the elliptic equation gradient with either Pt loading gradient change or GDL porosity remains consistent value through normal distribution or vice versa. In the dual-variable group, the two factors - Pt loading and GDL porosity - vary simultaneously and follow the elliptic equation gradient at the beginning of the simulation, the points after permutation and combination follow the Eq. (32), (33), (36) and (37), as can be seen in Fig. 1 at different starting points.

3.1 Single-variable analysis

The current uniformity over the entire electrode surface area is used to evaluate the homogeneity of current distribution. The GDL is firstly fixed at 0.7 with the homogeneous distribution. The gradient change of Pt loading from $m_{Pt,1}$ (point B of Fig. 1) to $m_{Pt,2}$ (point F of Fig. 1) are used to obtain the value of current density and its coefficient of variation under the condition that follows Eq. (31) and (35) at the cell voltage of 0.1 V. Case 1 to case 4 in Fig. 5

(a) are the results of current density distribution concerning the effect of a single variable that Pt loading increases from 0.1 to 0.4 mg cm^{-2} at point A in Fig. 1, and it can be seen the current density decreases with the increasing Pt loading with steady gradient change. It also can be noticed that the highest current density ~3.627 A cm^{-2} is obtained from case 2, with 0.2 mg cm^{-2} Pt loading implemented at the membrane-CL interface at the cathode inlet (point A of Fig. 1) and the CL-GDL interface at the cathode inlet (point B of Fig. 1). The dark red colour area in case 2 is the largest among the 4 cases, indicating that Pt loading at 0.2 mg cm^{-2} will lead to the highest current density. It is also found that the current density has different sensitivities to the gradient of Pt loading in different directions. Taking case 1 as an example, the current density presents a more sensitive response to the Pt loading gradient along the through-plane direction (from membrane to channel), and the maximum current density is obtained at the centre of the red coloured area follows by gradually decreasing around that point which meets the maximum value of current density. Comparing the change of current density in case 1 to case 4, it is proven that the maximum current density could be achieved through a reasonable control of the gradient along in-plane and through-plane direction when the Pt loading is 0.1 mg cm^{-2} in the inlet near to the membrane-CL interface (Point A). However, the current density can only be
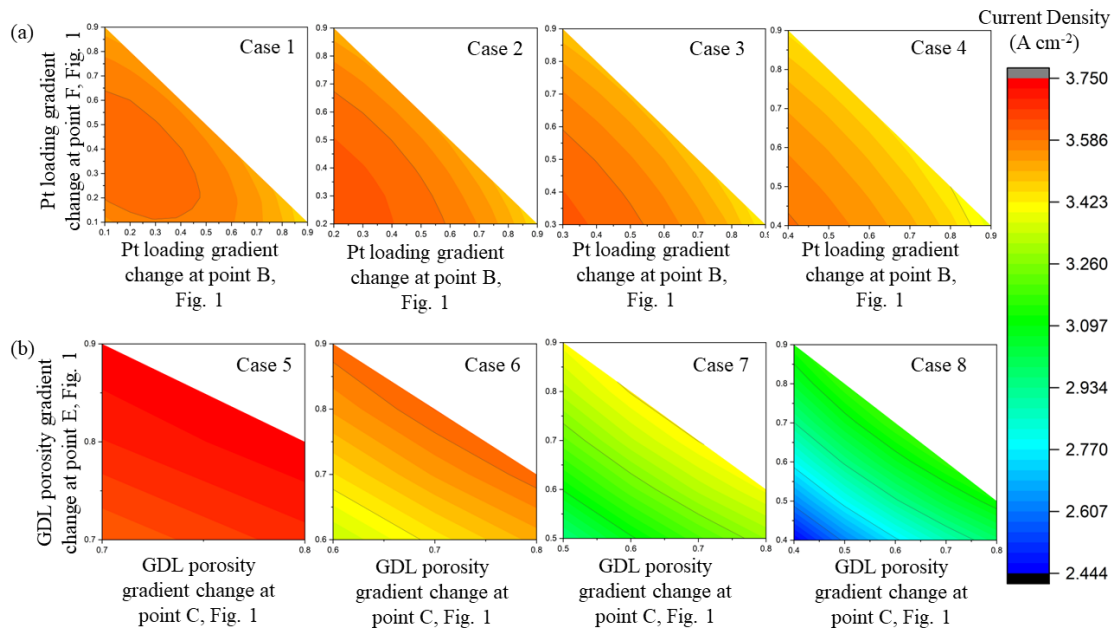

Figure 5 Effect of single factor variable on current density at 0.1 V. (a) Current density with constant GDL porosity (= 0.7) and graded Pt loading. Case 1 to case 4 indicate the Pt loading at point A of Fig. 1 changed from 0.1 mg cm^{-2} to 0.4 mg cm^{-2}. (b) Current density with graded GDL porosity while Pt loading is uniform (= 0.4 mg cm^{-2}). Case 5 to case 8 means that the porosity at point B of Fig. 1 changes from 0.7 to 0.4). details in Table S1 and Table S2 in SI

improved when the Pt loading in both in-plane and through-plane direction decrease when higher Pt loading is applied at Point A.

In case 5 to 8, the Pt loading remains constant over the electrode surface with a value of 0.4 mg cm^{-2}, only the GDL porosity changes obeying an elliptic function. Compared with the graded Pt loading case, the changes in GDL porosity show a linear trend. At the cell voltage of 0.1 V, the maximum current density increases with increasing GDL porosity. The current density is also affected by the gradient changes of GDL porosity along with different directions, in which a larger current density could be achieved when the porosity gradient increases along the in-plane direction (from gas inlet to the outlet), but the trend is relatively gentle. This implies that the reactant mass transport is reinforced by the higher GDL porosity so that a higher current density is achieved in the mass transport control zone.

Fig. 6a and 6d are the current uniformity in case 1 to case 8. The graded Pt loading and GDL porosity are separately studied in case 1-4 and case 5-8, respectively. In case 1 to case 4, the Pt loading is defined as a graded distribution with GDL porosity remaining constant at 0.7. It is clear in case 3 and case 4 that the distribution of current density is relatively inhomogeneous with high Pt loading between Point A and Point B. However, in case 1 and case 2, the Pt loading
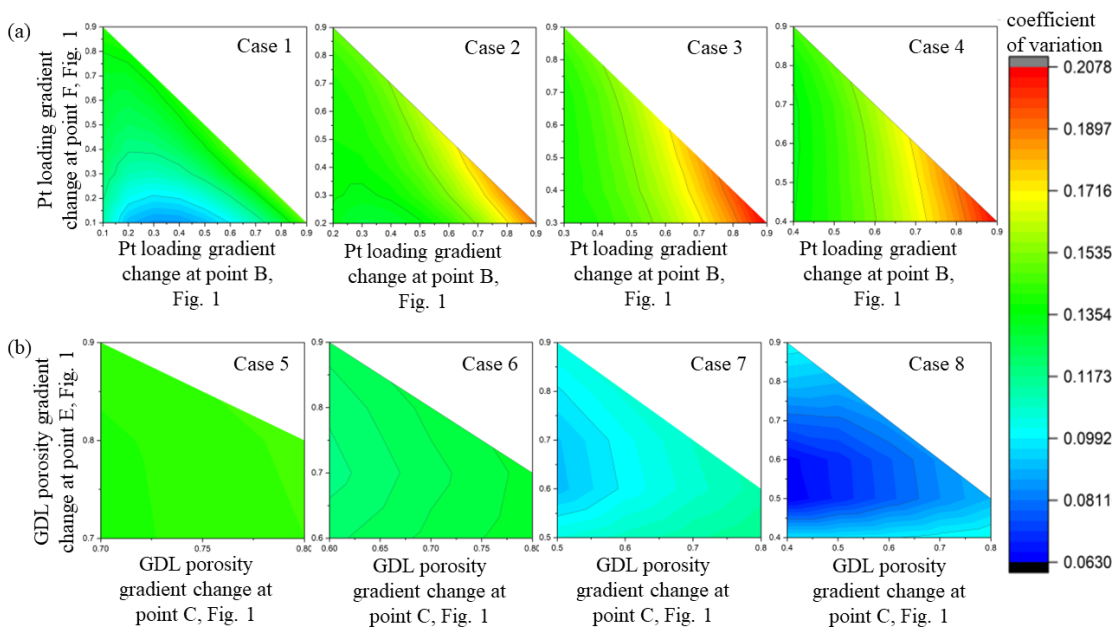

Figure 6 Effect of single factor variable on current density at 0.1 V. (a) The current coefficient of variation with constant GDL porosity (= 0.7) and graded Pt loading. (b) The current coefficient of variation with graded GDL porosity and uniform Pt loading (= 0.4 mg cm^{-2}). Details in Table S1 and Table S2 in SI

24

at Point B has an optimal value that induces a uniform current density distribution, and the range of these optimal values decreases when the Pt loading increases at Point A in Fig. 1. A more uniform current density distribution is received by reasonably changing the gradient of Pt loading in the in-plane and through-plane direction, when the Pt loading at the cathode inlet is lower along with the membrane-CL interface (from Point A to Point F in Fig. 1). However, if the Pt loading has a high value at the inlet near the membrane-CL interface (Point A in Fig 1), it is difficult to accomplish a uniform current density distribution even though the gradient change of Pt loading is controlled. This phenomenon can be explained by the fact that increasing Pt loading along the in-plane direction improves the reaction rate of ORR, leading to a high current density when the Pt loading at Point A is low (case 1 and case 2). On the other hand, CL porosity decreases significantly with high Pt loading, this results in a drop in current density at the outlet (details in Fig 5 (a) case 4) and reduces the uniformity of current density distribution over the entire electrode surface. The decrease of uniformity of current density is more obvious when Pt loading is high at Point A. Along the though-plane direction, moderate Pt loading increase at the CL-GDL interface (from Point B to Point E in Fig. 1) is beneficial to obtaining the higher current density. Meanwhile, when Pt loading is lower at point A, it can also enhance the uniformity of current density distribution. On the contrary, the increase in Pt loading at Point A results in a more uniform current dentistry distribution. This is because ORR mainly occurs along with the CL-GDL interface (from Point B to Point E in Fig. 1) when the Pt loading at this region is high, lower porosity also leads to Pt located in the CL near the membrane (From Point A to Point F in Fig. 1) not been fully utilised.

Fig. 6b is the situation with case 5-8, in which the GDL porosity is defined as a graded distribution with Pt loading remaining constant at 0.4 mg cm^{-2}. Different from the presentation in current density, the gradient change of GDL porosity with in-plane direction has an obvious impact on the uniformity of current density (first increases then decreases). Furthermore, enhancive initial porosity will bring the homogeneity down. Because the pore is blocked by the enrichment of water during the reaction process in GDL, which reduced the effective porosity. The porosity with an increased gradient changes lowers the impact of water on the porosity,

enhancing the homogeneity of current density. But improving initial porosity could drop the influence of gradient changes in the water.

3.2 Dual-variable analysis

The Pt loading and GDL porosity gradients are simultaneously considered in the dual-variable analysis. A big data pool with 5000 nodes is generated and 1000 nodes are selected for analysis based on the Latin hypercube algorithm. The sampling data obtained through solving a physics based COMSOL model are shown in Table S3 in SI, in which the current densities and their coefficient of variation are obtained at the cell voltage of 0.1 V.

The data is normalised after being imported into the RNN-LSTM ML algorithm, then split into training and testing sets with degrees of freedom is 30, which is to increase the randomness of the model to avoid the occurrence of fitting problem. The algorithm is run for ten rounds to avoid contingency, and the maximum current density and minimum current coefficient of variation are obtained for each result (details in Table S5 and Table S6 in SI).

Fig. 7 presents the result of R^2 and RMSE in current density and current coefficient of variation. The R^2 and RMSE of the current density are about 97.92% and 0.032, and the values for coefficient of variation are 67.38% and 0.129 (details in Table S7 and Table S8 in SI). It is observed that the RNN-LSTM algorithm has good performance in the prediction of current
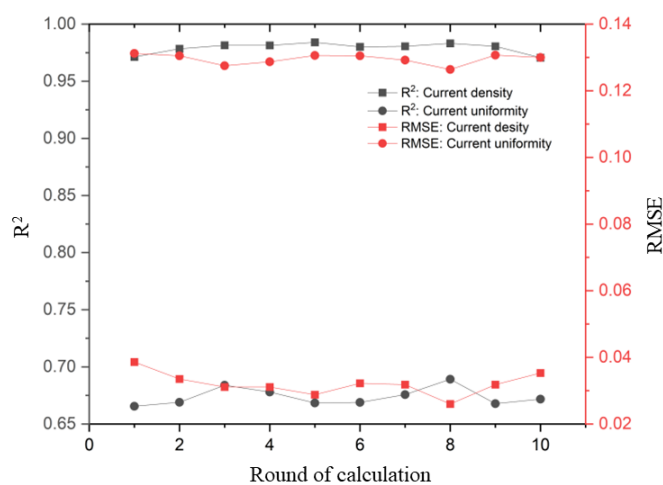

Figure 7 The change of R^2 and RMSE in current density and current uniformity with multiple rounds. The black line indicates the R^2 and the red line presents RMSE, where the data with square is the current density and the cycler is the current uniformity.

density (details in Fig. S1 in SI). For the coefficient of variation (details in Fig. S2 in SI), the values of R^2 are around 0.7 indicating that the current density has a stronger linear relationship between Pt loading and GDL than the coefficient of variation. While the RMSE is less than 0.2, which indicates a small error in this prediction result. the relative lower values of R^2 have an insignificant effect on the error in the prediction of this data.

Furthermore, comparing the data-driven surrogate model prediction and mechanistic simulation result shows that the maximum relative error in the current density is less than 5% and 17% for the current uniformity (details in Table S9 and Table S10 in SI). Moreover, it demonstrates that the coefficient of variation's result as the function of Pt loading and GDL porosity follows a nonlinear relationship. During the training process of the RNN-LSTM model, the output layer is co-prediction. Normalised linear data interact with each other, especially if the process of calculation to the output label has the same weight in the hidden layer, which means that the lower R^2 of coefficient of variation must reduce the R^2 for current density. However, the R^2 of the current density is very high (> 97%), indicating that the surrogate model has neither overfitting nor underfitting problems.

It is worthwhile to note that the discontinuous intervals of the dataset may reduce the prediction accuracy of the current uniformity. Although the R^2 of coefficient of variation is relatively low, the overall accuracy of the surrogate data-driven model is acceptable. Furthermore, the comparison of the R^2 and RMSE's changing trends in different rounds proves the stability of the algorithm.

Table 3 shows the results of the maximum current density and the best homogeneous current density distribution with multi-time calculations (details in Table S7 and Table S8 in SI), and COMSOL generated distribution of current density and its coefficient of variation profile are detailed in Fig. S3 and Fig. S4 in SI. It can be seen from the table that the distribution of Pt loading that can achieve the maximum current uniformity and current density are consistent, but the distribution of porosity is significantly different. Specifically, the maximum current density is obtained at the largest GDL porosity, but this brings a significant decrease in current uniformity. For example, when Pt loading at Point A, B and F are set to 0.1, 0.8 and 0.2 mg cm⁻

^{2}, the uniform distribution of porosity (= 0.8) over the GDL achieves the maximum current density (~ 3.869 A cm^{-2}), but the current coefficient of variation in this situation is 0.141. On the other hand, when the Pt loading distribution remains the same, the porosity distribution is 0.4 (Point B), 0.4 (Point C), and 0.8 (Point E), and the minimum current uniformity (~ 0.068) can be obtained with the current density of 3.018 A cm^{-2}. The change of porosity along the in-plane direction is the main reason that affects the uniformity of current density. The enhanced oxygen mass transfer near the cathode outlet with increasing porosity counteracts the effect of water enrichment on porosity and increases the current density in this region, thereby achieving a more uniform current density. However, the effect of the improvement in current density uniformity is to reduce the current density at 0.1 V, such as the predicted value (through surrogate model) of the current density decrease is 22% (from 3.869 A cm^{-2} to 3.018 A cm^{-2}), the calculated value (through mechanistic model) is 21% (from 3.716 A cm^{-2} to 2.950 A cm^{-2}), and the predicted value of current density distribution uniformity improved by 54% (from 0.149 to 0.068), the calculated value is 43% (from 0.141 to 0.080). From this work, the prediction of current density and current uniformity using an ML algorithm is reliable within the allowable error range and can be used for reference in simulation and experimental preparation. Such research outcome is not only useful for CL layer design but also particularly meaningful for electrode design and fabrication, as the synergy effect between CL and GDL has never been considered due to the difficulty of making property changes within the GDL practically. However, we are using ML assisted numerical experimental prediction for practical applications, by making appropriate GDL and CL properties combination, generating a guidance on how the current density and current density distribution uniformity are increased, therefore improve the FC's overall performance.

Table 3 Comparison set of the predicted result

	Current density Prediction (A cm^{-2})	Coefficient of variation Prediction	Current density Simulation (A cm^{-2})	Coefficient of variation Simulation	relative error: current density	relative error: coefficient of variation
Round 10[a]	3.869	0.149	3.716	0.141	0.041	0.053
Round 10[b]	3.018	0.068	2.950	0.080	0.023	-0.148

[a] indicates the maximum current density.
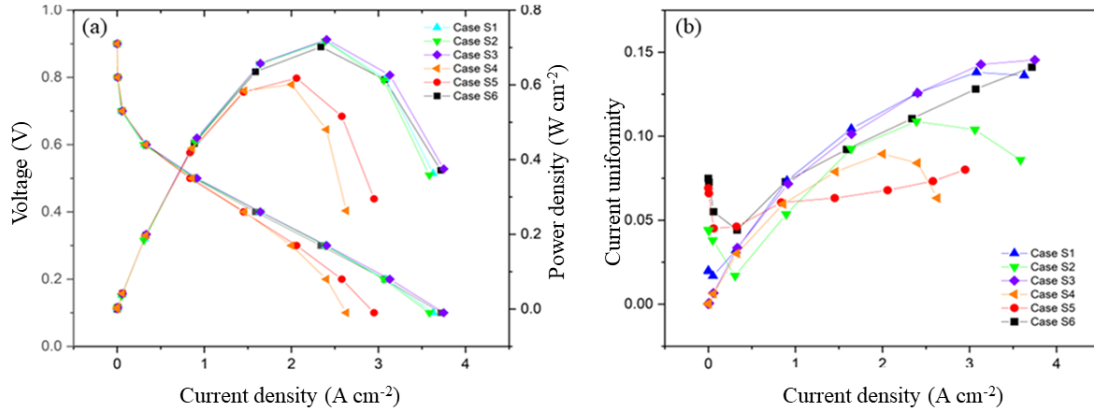[b] is the minimum coefficient of variation of current.

Figure 8 (a) Polarisation curves and (b) current coefficient of variation at various cell voltages

The data of Fig. 8 is obtained through the post-processing of the results in Fig. 5, Fig. 6, and Table 3, corresponding to the maximum current density and current uniformity in single-variable and dual-variable cases, respectively. Case S1 is the maximum current density (distribution of Pt loading are 0.2 mg cm^{-2}, 0.2 mg cm^{-2}, 0.3 mg cm^{-2} at Point A, B and F in Fig 1, respectively). Case S2 indicates the minimum current uniformity (distribution of Pt loading are 0.1 mg cm^{-2}, 0.3 mg cm^{-2}, 0.1 mg cm^{-2} at Point A, B and F, respectively), in which the Pt loading is a variable, and the porosity of GDL is fixed to 0.7. Case S3 represents the maximum current density (distribution of porosity are 0.7, 0.8, 0.8 at Point B, C and E, respectively). Case S4 denotes the minimum current coefficient of variation (distribution of porosity are 0.4, 0.4, 0.5 at Point B, C and E, respectively), in which the Pt loading is fixed at 0.4 mg cm^{-2} and GDL porosity is a variable. Case S5 indicates the maximum current density (Round 10[a] in Table 3) and Case S6 represents the minimum coefficient of variation (Round 10[b] in Table 3) for the dual-variable cases. The details of these six conditions are shown in Fig. S3 and Fig. S4 in SI. Fig. 8a shows the polarisation curves for the single-variable cases and dual-variable cases at the cell voltages in the range of 0.9 to 0.1 V. It is clear that the graded GDL porosity has a great impact on the current density than the graded Pt loading in the single-variable cases, i.e., the highest (Case S3) and lowest (Case S4) current density both occur with the applied conditions of graded GDL porosity and homogeneous Pt loading. Moreover, the current density in the dual-variable cases achieves the maximum uniformity (Case S6), which is higher than the

single-variable cases with graded GDL porosity and uniform Pt loading (Case S4). It means that the gradient Pt loading effectively reduces the influence of GDL porosity on current density. Furthermore, the highest power densities are observed at 0.3 V (Case S1 is 0.718 W cm^{-2}, Case S2 is 0.717 W cm^{-2}, Case S3 is 0.722 W cm^{-2}, Case S4 is 0.600 W cm^{-2}, Case S5 is 0.702 W cm^{-2}, Case S6 is 0.618 W cm^{-2}). On the other hand, the difference in current density is negligible between the dual-variable model (Case S5) and the single-variable (Case S1, Case S3), while all of them achieve the maximum current densities. The results present that the dual-variable model reaches a similar performance as a single variable model, while the lower Pt usage as received. The current coefficient of variation with the different conditions at a voltage from 0.1 to 0.9 V is shown in Fig. 8b. Comparing the result of current uniformity between dual-variable and the single-variable cases. The current uniformity is suboptimal at all voltages with the dual-variable model, while the change of trend is more smoothly.

4. Conclusion

In this research, the graded Pt loading and GDL porosity along the in-plane and through-plane directions over the electrode are investigated to improve the cell performance and homogeneity of the current density in a typical PEMFC. A two-dimensional, along-the-channel, multi-physics, two-phase flow, a non-isothermal mechanistic model was developed and implemented to generate a database for the developed data-driven surrogate model based on the recurrent neural network - long and short-term memory (RNN-LSTM) machine learning (ML) algorithm. The graded distribution of Pt loading and GDL porosity are individually (single-variable) and simultaneously (dual-variable), respectively.

In the single-variable analysis, when the GDL porosity is fixed at 0.7, a higher current density is achieved when the Pt loading is low at point A and gently increases towards the cathode outlet along the in-plane direction. When the platinum loading is fixed as a constant within the CL, the uniform distribution of GDL porosity at its maximum value achieves the highest current density at 0.1 V. More homogenous current density distribution is obtained while low Pt loading (e.g., 0.1 mg cm^{-2}, 0.2 mg cm^{-2}) is applied at the membrane-CL interface at the cathode inlet

(Point A in Fig. 1) with a small gradient along the through-plane direction. A low GDL porosity at Point A with a small gradient along the in-plane direction is also required for improving the homogeneity of the current density distribution.

When the two variables are considered simultaneously, the maximum current density is obtained if the following conditions are met: 1). uniformly distribution of porosity across the GDL (= 0.8), 2). The small gradient of Pt loading along the through-plane direction (i.e., from 0.1 to 0.2 mg cm^{-2}), 3). large gradient of Pt loading along the in-plane direction (i.e., from 0.1 to 0.8 mg cm^{-2}). When the Pt loading profile maintains unchanged, the average GDL porosity needs to be reduced to 0.53 (nonuniform distribution of 0.4, 0.4, and 0.8 at Point B, C and E) to minimise the current uniformity. Although the current density decreases by 22%, the current distribution uniformity increases by 54%.

The GDL porosity has a significant impact on the current density and current uniformity, where gradient Pt loading can reduce the negative influence from porosity changes. Therefore, the dual-variable model which achieves relatively high current density, low platinum consumption, and smoothed current uniformity.

The accuracy analysis of the developed RNN-LSTM ML surrogate model shows that the average value of R^2 and RMSE are 97.92% and 0.0320 for current density prediction, 67.38% and 0.1295 for current uniformity prediction, respectively. The maximum average error between the predicted value of the surrogate model and the calculated value of the physical model are 4.80% for current density and 16.60% for current uniformity (details in Table S9 and Table S10). Therefore, compared with the traditional simulation model, the data-driven model satisfied the requirement of accuracy while reducing the computing time.

Acknowledgments

Declaration of interests

There are no conflicts to declare.

Reference

(1) Wang, Y.; Chen, K. S.; Mishler, J.; Cho, S. C.; Adroher, X. C. A review of polymer electrolyte membrane fuel cells: Technology, applications, and needs on fundamental research. *Applied Energy* **2011**, *88* (4), 981-1007. DOI: https://doi.org/10.1016/j.apenergy.2010.09.030.

(2) Wang, J. Barriers of scaling-up fuel cells: Cost, durability and reliability. *Energy* **2015**, *80*, 509-521. DOI: https://doi.org/10.1016/j.energy.2014.12.007.

(3) Lü, X.; Qu, Y.; Wang, Y.; Qin, C.; Liu, G. A comprehensive review on hybrid power system for PEMFC-HEV: Issues and strategies. *Energy Conversion and Management* **2018**, *171*, 1273-1291. DOI: https://doi.org/10.1016/j.enconman.2018.06.065.

(4) Hordé, T.; Achard, P.; Metkemeijer, R. PEMFC application for aviation: Experimental and numerical study of sensitivity to altitude. *International Journal of Hydrogen Energy* **2012**, *37* (14), 10818-10829. DOI: https://doi.org/10.1016/j.ijhydene.2012.04.085.

(5) Gencoglu, M. T.; Ural, Z. Design of a PEM fuel cell system for residential application. *International Journal of Hydrogen Energy* **2009**, *34* (12), 5242-5248. DOI: https://doi.org/10.1016/j.ijhydene.2008.09.038.

(6) Lim, J. W.; Lee, D.; Kim, M.; Choe, J.; Nam, S.; Lee, D. G. Composite structures for proton exchange membrane fuel cells (PEMFC) and energy storage systems (ESS): Review. *Composite Structures* **2015**, *134*, 927-949. DOI: https://doi.org/10.1016/j.compstruct.2015.08.121.

(7) Xing, L.; Shi, W.; Su, H.; Xu, Q.; Das, P. K.; Mao, B.; Scott, K. Membrane electrode assemblies for PEM fuel cells: A review of functional graded design and optimization. *Energy* **2019**, *177*, 445-464. DOI: https://doi.org/10.1016/j.energy.2019.04.084.

(8) Liu, X.; Yu, E. H.; Scott, K. Preparation and evaluation of a highly stable palladium yttrium platinum core–shell–shell structure catalyst for oxygen reduction reactions. *Applied Catalysis B: Environmental* **2015**, *162*, 593-601. DOI: https://doi.org/10.1016/j.apcatb.2014.07.038.

(9) Liu, X.; Wu, X.; Scott, K. Study of niobium and tantalum doped titania-supported Pt electrocatalysts for methanol oxidation and oxygen reduction reactions. *Catalysis Science & Technology* **2014**, *4* (11), 3891-3898.

(10) Owejan, J. P.; Owejan, J. E.; Gu, W. Impact of Platinum Loading and Catalyst Layer Structure on PEMFC Performance. *Journal of The Electrochemical Society* **2013**, *160* (8), F824-F833. DOI: 10.1149/2.072308jes.

(11) Wee, J.-H.; Lee, K.-Y.; Kim, S. H. Fabrication methods for low-Pt-loading electrocatalysts in proton exchange membrane fuel cell systems. *Journal of Power Sources* **2007**, *165* (2), 667-677. DOI: https://doi.org/10.1016/j.jpowsour.2006.12.051.

(12) Liu, X.; Peng, F.; Lou, G.; Wen, Z. Liquid water transport characteristics of porous diffusion media in polymer electrolyte membrane fuel cells: A review. *Journal of Power Sources* **2015**, *299*, 85-96. DOI: https://doi.org/10.1016/j.jpowsour.2015.08.092.

(13) Ramousse, J.; Deseure, J.; Lottin, O.; Didierjean, S.; Maillet, D. Modelling of heat, mass and charge transfer in a PEMFC single cell. *Journal of Power Sources* **2005**, *145* (2), 416-427. DOI: https://doi.org/10.1016/j.jpowsour.2005.01.067.

(14) Pant, L. M.; Mitra, S. K.; Secanell, M. A generalized mathematical model to study gas transport in PEMFC porous media. *International Journal of Heat and Mass Transfer* **2013**, *58* (1), 70-79. DOI: https://doi.org/10.1016/j.ijheatmasstransfer.2012.11.023.

(15) Antoine, O.; Bultel, Y.; Ozil, P.; Durand, R. Catalyst gradient for cathode active layer of proton exchange membrane fuel cell. *Electrochimica Acta* **2000**, *45* (27), 4493-4500.

(16) Taylor, A. D.; Kim, E. Y.; Humes, V. P.; Kizuka, J.; Thompson, L. T. Inkjet printing of carbon supported platinum 3-D catalyst layers for use in fuel cells. *Journal of Power Sources* **2007**, *171* (1), 101-106. DOI: https://doi.org/10.1016/j.jpowsour.2007.01.024.

(17) Matsuda, H.; Fushinobu, K.; Ohma, A.; Okazaki, K. Structural Effect of Cathode Catalyst Layer on the Performance of PEFC. *Journal of Thermal Science and Technology* **2011**, *6* (1), 154-163. DOI: 10.1299/jtst.6.154.

(18) Kongstein, O. E.; Berning, T.; Børresen, B.; Seland, F.; Tunold, R. Polymer electrolyte fuel cells based on phosphoric acid doped polybenzimidazole (PBI) membranes. *Energy* **2007**, *32* (4), 418-422. DOI: https://doi.org/10.1016/j.energy.2006.07.009.

(19) Su, H.; Liang, H.; Bladergroen, B. J.; Linkov, V.; Pollet, B. G.; Pasupathi, S. Effect of Platinum Distribution in Dual Catalyst Layer Structured Gas Diffusion Electrode on the Performance of High Temperature PEMFC. *Journal of The Electrochemical Society* **2014**, *161* (4), F506-F512. DOI:

10.1149/2.077404jes.

(20) Roshandel, R.; Ahmadi, F. Effects of catalyst loading gradient in catalyst layers on performance of polymer electrolyte membrane fuel cells. *Renewable Energy* **2013**, *50*, 921-931. DOI: https://doi.org/10.1016/j.renene.2012.08.040.

(21) Srinivasarao, M.; Bhattacharyya, D.; Rengaswamy, R. Optimization studies of a polymer electrolyte membrane fuel cell with multiple catalyst layers. *Journal of Power Sources* **2012**, *206*, 197-203. DOI: https://doi.org/10.1016/j.jpowsour.2012.01.135.

(22) Prasanna, M.; Cho, E. A.; Kim, H. J.; Oh, I. H.; Lim, T. H.; Hong, S. A. Performance of proton-exchange membrane fuel cells using the catalyst-gradient electrode technique. *Journal of Power Sources* **2007**, *166* (1), 53-58. DOI: https://doi.org/10.1016/j.jpowsour.2006.12.076.

(23) Xing, L.; Wang, Y.; Das, P. K.; Scott, K.; Shi, W. Homogenization of current density of PEM fuel cells by in-plane graded distributions of platinum loading and GDL porosity. *Chemical Engineering Science* **2018**, *192*, 699-713. DOI: https://doi.org/10.1016/j.ces.2018.08.029.

(24) Therdthianwong, A.; Manomayidthikarn, P.; Therdthianwong, S. Investigation of membrane electrode assembly (MEA) hot-pressing parameters for proton exchange membrane fuel cell. *Energy* **2007**, *32* (12), 2401-2411. DOI: https://doi.org/10.1016/j.energy.2007.07.005.

(25) Sun, W.; Peppley, B. A.; Karan, K. Modeling the Influence of GDL and flow-field plate parameters on the reaction distribution in the PEMFC cathode catalyst layer. *Journal of Power Sources* **2005**, *144* (1), 42-53. DOI: https://doi.org/10.1016/j.jpowsour.2004.11.035.

(26) Lim, C.; Wang, C. Y. Effects of hydrophobic polymer content in GDL on power performance of a PEM fuel cell. *Electrochimica Acta* **2004**, *49* (24), 4149-4156. DOI: https://doi.org/10.1016/j.electacta.2004.04.009.

(27) Rama, P.; Liu, Y.; Chen, R.; Ostadi, H.; Jiang, K.; Gao, Y.; Zhang, X. X.; Fisher, R.; Jeschke, M. Simulation of liquid water breakthrough in a nanotomography reconstruction of a carbon paper gas-diffusion layer. *AIChE Journal* **2012**, *58* (2), 646-655, https://doi.org/10.1002/aic.12581. DOI: https://doi.org/10.1002/aic.12581 (acccessed 2022/02/18).

(28) Chu, H.-S.; Yeh, C.; Chen, F. Effects of porosity change of gas diffuser on performance of proton exchange membrane fuel cell. *Journal of Power Sources* **2003**, *123* (1), 1-9. DOI: https://doi.org/10.1016/S0378-7753(02)00605-5.

(29) Roshandel, R.; Farhanieh, B.; Saievar-Iranizad, E. The effects of porosity distribution variation on PEM fuel cell performance. *Renewable Energy* **2005**, *30* (10), 1557-1572. DOI: https://doi.org/10.1016/j.renene.2004.11.017.

(30) Chen, F.; Chang, M.-H.; Hsieh, P.-T. Two-phase transport in the cathode gas diffusion layer of PEM fuel cell with a gradient in porosity. *International Journal of Hydrogen Energy* **2008**, *33* (10), 2525-2529. DOI: https://doi.org/10.1016/j.ijhydene.2008.02.077.

(31) Huang, Y.-X.; Cheng, C.-H.; Wang, X.-D.; Jang, J.-Y. Effects of porosity gradient in gas diffusion layers on performance of proton exchange membrane fuel cells. *Energy* **2010**, *35* (12), 4786-4794. DOI: https://doi.org/10.1016/j.energy.2010.09.011.

(32) Zhan, Z.; Xiao, J.; Li, D.; Pan, M.; Yuan, R. Effects of porosity distribution variation on the liquid water flux through gas diffusion layers of PEM fuel cells. *Journal of Power Sources* **2006**, *160* (2), 1041-1048. DOI: https://doi.org/10.1016/j.jpowsour.2006.02.060.

(33) Zhan, Z.; Xiao, J.; Zhang, Y.; Pan, M.; Yuan, R. Gas diffusion through differently structured gas diffusion layers of PEM fuel cells. *International Journal of Hydrogen Energy* **2007**, *32* (17), 4443-4451. DOI: https://doi.org/10.1016/j.ijhydene.2007.03.041.

(34) Lim, I. S.; Park, J. Y.; Kang, D. G.; Choi, S. H.; Kang, B.; Kim, M. S. Numerical study for in-plane gradient effects of cathode gas diffusion layer on PEMFC under low humidity condition. *International Journal of Hydrogen Energy* **2020**, *45* (38), 19745-19760. DOI: https://doi.org/10.1016/j.ijhydene.2020.05.048.

(35) Wang, Y.; Wang, X.; Qin, Y.; Zhang, L.; Wang, Y. Three-dimensional numerical study of a cathode gas diffusion layer with a through/in plane synergetic gradient porosity distribution for PEM fuel cells. *International Journal of Heat and Mass Transfer* **2022**, *188*, 122661. DOI: https://doi.org/10.1016/j.ijheatmasstransfer.2022.122661.

(36) Adithya Legala and Jian Zhao and Xianguo, L. Machine learning modeling for proton exchange membrane fuel cell performance. *Energy and AI* **2022**, *10*, 100183. DOI: https://doi.org/10.1016/j.egyai.2022.100183.

(37) Mehrpooya, M.; Ghorbani, B.; Jafari, B.; Aghbashlo, M.; Pouriman, M. Modeling of a single cell micro proton exchange membrane fuel cell by a new hybrid neural network method. *Thermal Science and Engineering Progress* **2018**, *7*, 8-19. DOI: https://doi.org/10.1016/j.tsep.2018.04.012.

(38) Han, I.-S.; Chung, C.-B. Performance prediction and analysis of a PEM fuel cell operating on pure oxygen using data-driven models: A comparison of artificial neural network and support vector machine. *International Journal of Hydrogen Energy* **2016**, *41* (24), 10202-10211. DOI: https://doi.org/10.1016/j.ijhydene.2016.04.247.

(39) Gu, G. H.; Noh, J.; Kim, I.; Jung, Y. Machine learning for renewable energy materials. *Journal of Materials Chemistry A* **2019**, *7* (29), 17096-17117.

(40) Kheirandish, A.; Motlagh, F.; Shafiabady, N.; Dahari, M. Dynamic modelling of PEM fuel cell of power electric bicycle system. *International Journal of Hydrogen Energy* **2016**, *41* (22), 9585-9594. DOI: https://doi.org/10.1016/j.ijhydene.2016.02.046.

(41) Kheirandish, A.; Shafiabady, N.; Dahari, M.; Kazemi, M. S.; Isa, D. Modeling of commercial proton exchange membrane fuel cell using support vector machine. *International Journal of Hydrogen Energy* **2016**, *41* (26), 11351-11358. DOI: https://doi.org/10.1016/j.ijhydene.2016.04.043.

(42) Kheirandish, A.; Motlagh, F.; Shafiabady, N.; Dahari, M.; Khairi Abdul Wahab, A. Dynamic fuzzy cognitive network approach for modelling and control of PEM fuel cell for power electric bicycle system. *Applied Energy* **2017**, *202*, 20-31. DOI: https://doi.org/10.1016/j.apenergy.2017.05.084.

(43) Wang, B.; Xie, B.; Xuan, J.; Jiao, K. AI-based optimization of PEM fuel cell catalyst layers for maximum power density via data-driven surrogate modeling. *Energy Conversion and Management* **2020**, *205*, 112460. DOI: https://doi.org/10.1016/j.enconman.2019.112460.

(44) Xing, L.; Liu, X.; Alaje, T.; Kumar, R.; Mamlouk, M.; Scott, K. A two-phase flow and non-isothermal agglomerate model for a proton exchange membrane (PEM) fuel cell. *Energy* **2014**, *73*, 618-634. DOI: https://doi.org/10.1016/j.energy.2014.06.065.

(45) Xing, L.; Xu, Y.; Penga, Ž.; Xu, Q.; Su, H.; Barbir, F.; Shi, W.; Xuan, J. A segmented fuel cell unit with functionally graded distributions of platinum loading and operating temperature. *Chemical Engineering Journal* **2021**, *406*, 126889. DOI: https://doi.org/10.1016/j.cej.2020.126889.

(46) Barbir, F. *PEM fuel cells: theory and practice*; Academic press, 2012.

(47) Sun, W.; Peppley, B. A.; Karan, K. An improved two-dimensional agglomerate cathode model to study the influence of catalyst layer structural parameters. *Electrochimica Acta* **2005**, *50* (16), 3359-3374. DOI: https://doi.org/10.1016/j.electacta.2004.12.009.

(48) Shah, A. A.; Kim, G. S.; Sui, P. C.; Harvey, D. Transient non-isothermal model of a polymer electrolyte fuel cell. *Journal of Power Sources* **2007**, *163* (2), 793-806. DOI: https://doi.org/10.1016/j.jpowsour.2006.09.022.

(49) Kamarajugadda, S.; Mazumder, S. Numerical investigation of the effect of cathode catalyst layer structure and composition on polymer electrolyte membrane fuel cell performance. *Journal of Power Sources* **2008**, *183* (2), 629-642. DOI: https://doi.org/10.1016/j.jpowsour.2008.05.072.

(50) Khajeh-Hosseini-Dalasm, N.; Fesanghary, M.; Fushinobu, K.; Okazaki, K. A study of the agglomerate catalyst layer for the cathode side of a proton exchange membrane fuel cell: Modeling and optimization. *Electrochimica Acta* **2012**, *60*, 55-65. DOI: https://doi.org/10.1016/j.electacta.2011.10.099.

(51) Xing, L.; Xu, Y.; Penga, Ž.; Xu, Q.; Su, H.; Shi, W.; Barbir, F. A novel flow field with controllable pressure gradient to enhance mass transport and water removal of PEM fuel cells. *AIChE Journal* **2020**, *66* (6), e16957.

(52) Xing, L.; Shi, W.; Das, P. K.; Scott, K. Inhomogeneous distribution of platinum and ionomer in the porous cathode to maximize the performance of a PEM fuel cell. *AIChE Journal* **2017**, *63* (11), 4895-4910.

(53) Pasaogullari, U.; Wang, C.-Y. Two-phase transport and the role of micro-porous layer in polymer electrolyte fuel cells. *Electrochimica Acta* **2004**, *49* (25), 4359-4369. DOI: https://doi.org/10.1016/j.electacta.2004.04.027.

(54) Wu, H.; Berg, P.; Li, X. Modeling of PEMFC Transients with Finite-Rate Phase-Transfer Processes. *Journal of The Electrochemical Society* **2010**, *157* (1), B1. DOI: 10.1149/1.3248005.

(55) Wu, H.; Berg, P.; Li, X. Steady and unsteady 3D non-isothermal modeling of PEM fuel cells with the effect of non-equilibrium phase transfer. *Applied Energy* **2010**, *87* (9), 2778-2784. DOI: https://doi.org/10.1016/j.apenergy.2009.06.024.

(56) Xing, L.; Song, X.; Scott, K.; Pickert, V.; Cao, W. Multi-variable optimisation of PEMFC cathodes based on surrogate modelling. *International Journal of Hydrogen Energy* **2013**, *38* (33), 14295-14313. DOI: https://doi.org/10.1016/j.ijhydene.2013.08.104.

(57) Xing, L.; Mamlouk, M.; Kumar, R.; Scott, K. Numerical investigation of the optimal Nafion® ionomer content in cathode catalyst layer: An agglomerate two-phase flow modelling. *International Journal of Hydrogen Energy* **2014**, *39* (17), 9087-9104. DOI: https://doi.org/10.1016/j.ijhydene.2014.03.225.

(58) Khajeh-Hosseini-Dalasm, N.; Kermani, M. J.; Moghaddam, D. G.; Stockie, J. M. A parametric study of cathode catalyst layer structural parameters on the performance of a PEM fuel cell. *International Journal of Hydrogen Energy* **2010**, *35* (6), 2417-2427. DOI: https://doi.org/10.1016/j.ijhydene.2009.12.111.

(59) Hochreiter, S.; Schmidhuber, J. Long Short-Term Memory. *Neural Computation* **1997**, *9* (8), 1735-1780. DOI: 10.1162/neco.1997.9.8.1735.

(60) Wang, L.; Husar, A.; Zhou, T.; Liu, H. A parametric study of PEM fuel cell performances. *International Journal of Hydrogen Energy* **2003**, *28* (11), 1263-1272. DOI: https://doi.org/10.1016/S0360-3199(02)00284-7.

(61) Spiess, A.-N.; Neumeyer, N. An evaluation of R2 as an inadequate measure for nonlinear models in pharmacological and biochemical research: a Monte Carlo approach. *BMC pharmacology* **2010**, *10* (1), 1-11.

(62) Abdi, M.; Ghalandarzadeh, A.; Shafiei-Chafi, L. Optimization of lime and fiber content for improvement of clays with different plasticity using response surface method (RSM). *Transportation Geotechnics* **2022**, *32*, 100685.